

Coarse-grained modeling of polymers with end-on and side-on liquid crystal moieties: effect of architecture

Diego Becerra,^{*,†} Pranav R. Jois,[‡] and Lisa M. Hall^{*,†}

[†]*William G. Lowrie Department of Chemical and Biomolecular Engineering, The Ohio State
University, Columbus, Ohio 43210, USA*

[‡]*Department of Mathematics and Department of Physics, The Ohio State University, Columbus,
Ohio 43210, USA*

E-mail: becerra.39@osu.edu; hall.1004@osu.edu

Abstract

Mesogens, which are typically stiff rodlike or disklike molecules, are able to self-organize into liquid crystal (LC) phases in a certain temperature range. Such mesogens, or LC groups, can be attached to polymer chains in various configurations including within the backbone (main-chain LC polymers) or at the ends of side-chains attached to the backbone in an end-on or side-on configuration (side-chain LC polymers or SCLCPs), which can display synergistic properties arising from both their LC and polymeric character. At lower temperatures, chain conformations may be significantly altered due to the mesoscale LC ordering, thus, when heating from the LC ordered state through the LC to isotropic phase transition, the chains return from a more stretched to a more random coil conformation. This can cause macroscopic shape changes, which depend significantly on the type of LC attachment and other architectural properties of the polymer. Here, to study the structure-property relationships for SCLCPs with a range of different architectures, we develop a coarse-grained model that includes torsional potentials along with LC interactions of a Gay-Berne form. We create systems of different side chain lengths, chain stiffnesses, and LC attachment types, and track their structural properties as a function of temperature. Our modeled systems indeed form a variety of well-organized mesophase structures at low temperatures, and we predict higher LC to isotropic transition temperatures for the end-on side-chain systems than for analogous side-on side-chain systems. Understanding these phase transitions and their dependence on polymer architecture can be useful in designing materials with reversible and controllable deformations.

INTRODUCTION

Liquid crystals (LCs) are stiff self-organizing molecules that can be attached to relatively flexible polymer chains either within the backbone or in an end-on or side-on configuration along the backbone, yielding a material that takes advantage of the properties of both types of materials. The backbone tends towards a random walk at high temperatures, but when the LC groups order at lower temperatures, the backbone is distorted and the material expands or contracts (depending on LC attachment) along the LC director. Though our focus here is on uncrosslinked systems, LC polymers can be lightly crosslinked to take greater advantage of such deformations on a macroscopic scale. Such LC elastomers (LCEs), with LC moieties attached to the chains in various ways, have been the focus of significant recent research.¹⁻³ Importantly, due to the stimuli-responsive nature of the LC groups, or mesogens, LCEs can be placed in a state with kinetically trapped polymer conformations with low conformational entropy, and they can later be prompted to return to their original state by an external stimulus.⁴⁻⁸ These types of shape changes can be leveraged in applications such as artificial muscles, as first proposed by de Gennes.⁹ With synthetic advances that allow for additional complexity and tunability in their deformation behavior, LCEs can now allow for a variety of controlled and reversible thermo- and photo-mechanical responses,¹⁰⁻¹² of interest in soft robotics, optical data storage, biomedicine, and tissue engineering.^{13-17,17-19}

Here, we model simplified systems of LC polymers (that are not cross-linked to make LCEs), focusing on how polymer architectural parameters lead to different microstructures that would then lead to different responses if made into an LCE material. In general, LCs can be attached to polymer chains either within the backbone, leading to main-chain LC polymers (MCLCPs), or in an end-on or side-on configuration at the ends of short polymeric segments (also called “spacers”) attached to the backbone, leading to side-chain LC polymers (SCLCPs). These spacers usually have a small number of repeat units and allow the polymer main backbone to accommodate the anisotropic orientation

of mesogenic side groups,²⁰ allowing for coupling/decoupling the constituent parts. Although these two types of LC polymers share conformational units, they are intrinsically different; compared with the well-studied MCLCPs,^{21–26} where mesogenic groups are the monomers that compose the polymer itself, in the SCLCPs, the structure of the polymer backbone, the grafting density of side chains, the LC type of attachment, the tacticity, and the spacer length all exert an important influence on the mesophase morphology.^{27,28}

At high enough temperatures, thermotropic LC polymers offer typical polymeric features such as elasticity, and their polymer chains approach a random coil configuration due to entropic considerations. However, at lower temperatures, the LC groups form ordered phases (e.g., nematic or smectic). This LC ordering occurs at the expense of lowering the polymeric conformational entropy, and the conformations of the flexible, non-LC polymer segments can be significantly stretched.

In this context, understanding the morphology, dynamics, and self-organization in SCLCP systems is of great fundamental and technological interest as has been demonstrated over the years through both experimental^{29–34} and theoretical^{35–43} studies, which have studied these systems’ phase diagrams, elastic properties, atomistic structuring, hydrodynamics, and classical rheology. A main characteristic of SCLCP systems, and one which makes them challenging to model, is the existence of orientational and possibly positional order of their constituent parts along with molecular scale features on different length scales, as well as the presence of transitions and sometimes coexistence between different phases. In this regard, simplified models can be useful in understanding the overall phase behavior of SCLCPs. In particular, Wang and Wang⁴⁴ applied a self-consistent-field theoretic approach to SCLCPs; their model takes into account the coupling between the orientation of the side-chain LC groups and that of the backbone segments, both locally and globally. One of the main takeaways is that for side-on SCLCPs, the coupling effects act cooperatively so that the chain conformation is always prolate, meaning that the polymer chains align in the same direction as the LC groups in the

LC mesophases. Instead, for the end-on SCLCPs, these effects act competitively and the chain conformation can be either prolate or oblate (meaning that the polymer chains are stretched perpendicular to the LC director in the LC mesophases).

Since adequate descriptions of SCLCP systems require consideration of both inter- and intra-molecular interactions and also system sizes large enough to effectively capture overall molecular ordering, coarse-grained molecular simulations are appropriate.^{45,46} Some attempts to model SCLCPs in prior works are based on hybrid models of spherically symmetrical and anisotropic sites.^{24,25,27,47–51} In particular Stimson and Wilson²⁷ proposes a coarse-grained model for SCLCP molecules which arises as an extension of a series of previous works on liquid crystal polymers from the same group.^{47–49} The model, which is meant to represent a specific chemical type of polymer with a polydimethylsiloxane backbone and flexible side chains terminated in mesogenic groups, includes harmonic bonds, dihedral potentials, Lennard-Jones (LJ) interactions for backbone beads, and anisotropic interactions for mesogenic groups (specifically, a Gay–Berne model^{52–54}). By applying a small aligning potential during a cooling processes from fully isotropic polymer melt, they found microphase formation, specifically, to a smectic-A phase, which is in good agreement with experimental scattering data. Later simulations by Ilnytskyi *et al.* provided further understanding of SCLCP systems.^{50,51,55} Using a similar modeling technique (semiatomistic level of description) as the previously mentioned group, they studied end-on SCLCP systems of a range of backbone and spacer lengths, giving rise to isotropic, polydomain smectic, and monodomain smectic phases, the latter by using an external alignment field. Also, they performed structural and dynamic analyses from equilibrium and non-equilibrium simulations using their in-house MD code.^{56,57}

In this work we also employ a coarse-grained model for SCLCPs, but with additional orientational interactions discussed below. We simulate both end-on SCLCP systems (as studied in previous simulation works) and side-on SCLCP systems (we believe for the first time) and analyze a range of structural phenomena. We aim to understand the

relationship between the molecular architecture, including LC type of attachment, and the morphology of any ordered phases. Our underlying polymeric model is inspired by an elastic rod model for semiflexible polymers that accounts for bending, orientational, and twisting interactions.^{58–60} By including these orientations, making a fully anisotropic model even for the spherical polymeric beads, we can capture a broader range of possible molecular architectures, including reproducing tacticity. Though the tracking of orientations and torques adds computational expense, we can still simulate relatively large systems on long timescales.

The paper is organized as follows. We first discuss the details of the SCLCP coarse-grained model and the simulation methodology (Sec.). In Sec. , the results obtained for different architectural parameters of the model and the corresponding mesophases formed in different thermodynamic states are presented and discussed. Finally, in Sec. we show some comparative computational performance results. The coarse-grained model is implemented in the open-source LAMMPS package⁶¹ and the particular external orientational alignment field discussed below is freely available online.⁶²

MODEL AND METHODOLOGY

Coarse-grained model

In our coarse-grained model for SCLCPs, the polymer backbone is represented by a twistable worm-like chain model,^{58,59} composed of spherical beads, to which pendant side chains are attached. In the current work, side chains are attached syndiotactically, with a grafting density of one side chain every other backbone bead. The side chains are composed of a number of spacer beads with the same model as backbone beads followed by a terminal mesogenic group modeled as an ellipsoid using a Gay–Berne (GB) potential,^{52–54} a generalization of the 12-6 Lennard-Jones (LJ) potential for anisotropic interactions. These LC moieties are attached in an end-on (with the long axis parallel to the last spacer bond)

or side-on (with the long axis perpendicular to the last spacer bond) configuration.

Orientations and angular momenta are tracked for all sites/beads using quaternions for computational efficiency. However, for an intuitive representation of the model and its potentials, here we discuss the orientation of each site in terms of an typical orthonormal basis in 3D,^{59,60} with the orientation of the i th site in the lab-frame being $(\hat{f}_i, \hat{v}_i, \hat{u}_i)$. A representation of two SCLCP molecules with different LC types of attachments is shown in Figure 1.

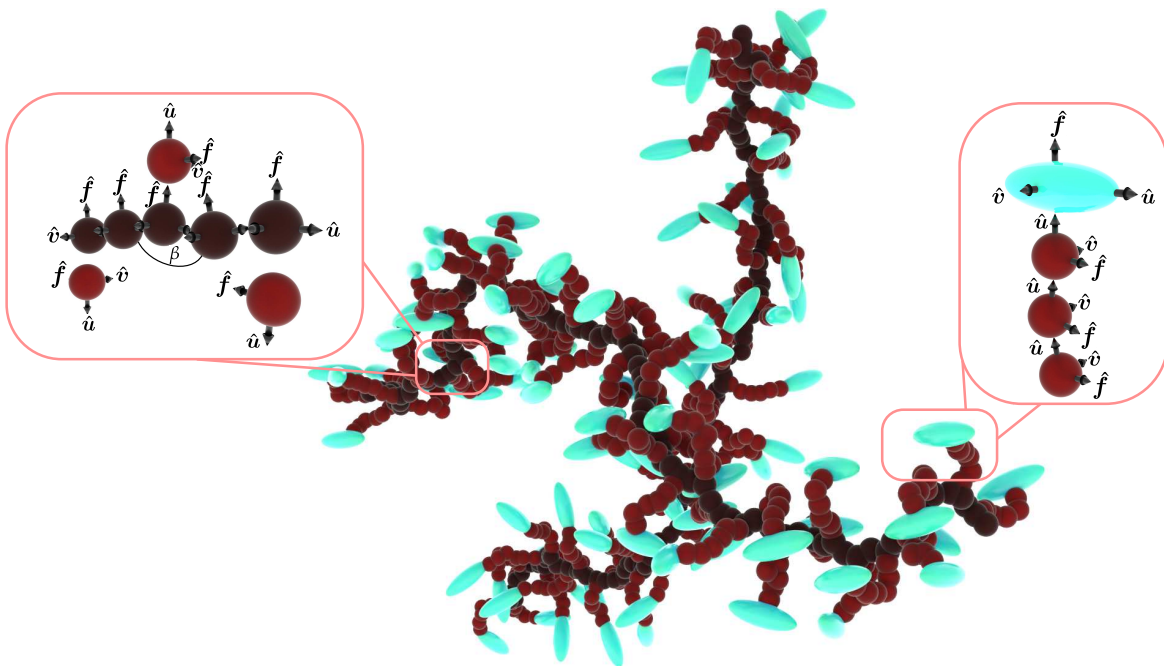


Figure 1: Representation of two side-chain liquid crystal polymer molecules, one containing purely end-on mesogenic groups and the other containing purely side-on mesogenic groups. Liquid crystals are modeled by ellipsoidal sites (cyan) attached to the spacer chains (scarlet), which in turn are attached to the polymer main backbone (dark scarlet). The left magnified image shows the first spacer beads orientationally attached to the backbone whereas the right magnified image shows a side-on liquid crystal moiety attached to the respective spacer. The \hat{f} , \hat{v} , \hat{u} unit vectors (arrows) denote the orientation of each anisotropic site. Images were rendered using Blender.⁶³

Nonbonded interactions

Pairwise interaction potentials exist between all nonbonded pairs of sites; since we use anisotropic sites, in some cases the interaction between particles i and j depends on both the distance and the orientation of particle i or j (or both). The specific interactions are: (i) a typical 12-6 Lennard-Jones (LJ) potential, $U_{\text{LJ}}(\mathbf{r}_{ij})$, if both sites involved are spherical, i.e., i and j correspond to either backbone beads or spacer beads; (ii) a Gay-Berne (GB) anisotropic potential,⁵² $U_{\text{GB}}(\hat{\mathbf{u}}_i, \hat{\mathbf{u}}_j, \mathbf{r}_{ij})$, if both sites involved in the interaction are aspherical, i.e., i and j correspond to LC moieties (we choose parameters to give prolate ellipsoids, longer in one axis than the others); and (iii) a cross term $U_{\text{GB/LJ}}(\hat{\mathbf{u}}_i, \mathbf{r}_{ij})$, which represents a generalized potential for two unlike Gay-Berne particles, if j corresponds to a spherical site and i to an aspherical site, or $U_{\text{GB/LJ}}(\hat{\mathbf{u}}_j, \mathbf{r}_{ij})$, if i corresponds to a spherical site and j to an aspherical site. Here, $\mathbf{r}_{ij} = \mathbf{r}_i - \mathbf{r}_j$ is the interparticle vector, and $\hat{\mathbf{u}}_i$ and $\hat{\mathbf{u}}_j$ are the unit vectors of the main axis of the mesogenic groups of sites i and j , respectively. Moreover, in this work, the parameters are described in dimensionless units in terms of the characteristic LJ length σ , energy ε , and mass m . For all spherical interactions, the mass, LJ energy, and LJ diameter parameters are set to unity to simulate a generic polymer. GB interactions^{52,64} between two anisotropic particles or between pairs of dissimilar particles are calculated using the formalism of Everaers and Ejtehadi⁶⁵ as implemented in LAMMPS⁶¹ with parameters as described below. For the sake of clarity, we briefly reproduce below the key equations, but for a deeper understanding, the reader should refer to the original sources.

The GB particle shape is controlled by the ellipsoidal semiaxes a_i , b_i , and c_i for each particle i , which form the diagonal elements of a “shape” matrix, $\mathbf{S}_i = \text{diag}(a_i, b_i, c_i)$. The relative well depths $\varepsilon_{a,i}$, $\varepsilon_{b,i}$, and $\varepsilon_{c,i}$ for each particle i give the matrix $\mathbf{E}_i = \text{diag}(\varepsilon_{a,i}, \varepsilon_{b,i}, \varepsilon_{c,i})$. We have the following relations:

$$\varepsilon_a = \sigma \cdot \frac{a}{b \cdot c}; \varepsilon_b = \sigma \cdot \frac{b}{a \cdot c}; \varepsilon_c = \sigma \cdot \frac{c}{a \cdot b}, \quad (1)$$

where a , b , and c control the shape of the ellipsoid in the side, face, and end-to-end dimensions, respectively. More precisely, a , b , and c are the separations at which the attractive and repulsive terms in the potential cancel when the molecules are in the side-by-side, face-to-face, and end-to-end configuration, respectively. On the other hand, ε_a , ε_b , and ε_c , are the well depths for the side-by-side, face-to-face, and end-to-end configurations, respectively.

The GB formula is,

$$U_{\text{GB}} = U_r \cdot \eta \cdot \chi. \quad (2)$$

Here, $U_r = 4\varepsilon(q^{12} - q^6)$, with $q = \frac{\sigma}{h_{ij} + \gamma\sigma}$, controls the shifted distance-dependent interaction based on the distance of the closest approach between particles ($h_{ij}(A_i, A_j, S_i, S_j, \mathbf{r}_{ij})$), where A_i and A_j are the transformation matrices from the simulation body-frame to the lab-frame and γ is the shift for potential minimum (here set to 1). Moreover, the interaction anisotropy is characterized by the terms $\eta(A_i, A_j, S_i, S_j, \nu)$ and $\chi(A_i, A_j, E_i, E_j, \hat{\mathbf{r}}_{ij}, \mu)$ that control interaction strength based on the particle shapes and relative well depths, respectively. The parameters μ and ν are empirically determined exponents that can be tuned to adjust the potential.

In this work, the liquid crystal units are modeled as uniaxial ellipsoids with a mass of $1.5m$, and GB parameters $\sigma = 1$, $\varepsilon = 1$, $a = b = \sigma$, $c = 3\sigma$, $\varepsilon_a = \varepsilon_b = \varepsilon$, and $\varepsilon_c = 0.2\varepsilon$. With these parameters, we can define the aspect ratio, $\kappa \equiv c/a$ of the particles (in this case is 3) and the energy anisotropy ratio, $\kappa' \equiv \varepsilon_a/\varepsilon_c$, in this case, set to 5.

From here, the GB potential has four adjustable parameters. In the compact notation of Bates and Luckhurst⁶⁶ these are $(\kappa, \kappa', \mu, \nu)$. The four parameters have been set to the original values⁵² (3, 5, 2, 1) in several studies.⁶⁷⁻⁷⁰ A second set of parameters, (3, 5, 1, 2), was studied by Luckhurst et al.⁷¹; here, the existence of smectic, nematic, and isotropic phases was demonstrated, while the behavior inside the phases was not studied in detail. This set of parameters was also implemented in side-chain liquid crystalline

polymer studies.^{50,51} A third set of parameters that enhance the side-by-side and end-to-end interactions between the particles has been used by Berardi *et al.*,^{26,72} (3, 5, 1, 3). This set has also been used by Brown *et al.*⁷³ for studying liquid crystal nanodroplets in solution. A final type of selected Gay–Berne potential that we are aware of is the one proposed by Bates and Luckhurst⁶⁶ and also implemented in Margola *et al.*⁷⁴, (4.4, 20, 1, 1). With this choice, the mesogens are closer to elongated molecules because the parametrization has larger anisotropic ratios than the other sets. In this work, we have adopted the parametrization proposed by Berardi *et al.*⁷², (3, 5, 1, 3). The values of the parameters used in the $U_{\text{nonbonded}}$ are given in the supplementary material.

Bond and angle interactions

Since all sites in the model have both a position and an orientation, the bond and angle interactions in the SCLCP model can control the mesogenic type of attachment, type of tacticity, among other constraints that involve relative position and relative orientation of bonded sites. To explain the intramolecular potentials, we separate them into potentials within the polymer backbone and the spacers, between the polymer backbone and spacers, and between the spacers and liquid crystals moieties (see Figure 2). From now on, the notation employed for intramolecular potentials is the same as in Lequieu *et al.*⁶⁰.

Interactions within the polymer (main backbone and spacers) are represented by a twistable worm-like chain model.^{58–60} These flexible polymer chains consist of N_b beads, and the potential energy is given by

$$\begin{aligned}
& U_{\text{bond}} + U_{\text{angle}} + U_{\text{twist}} + U_{\text{align}} \\
&= \frac{k_b}{2} \sum_{i=1}^{N_b-1} (\ell_i - \ell_{b,0})^2 + k_\beta \sum_{i=1}^{N_b-2} [1 - \cos(\beta_i)] \\
&\quad + k_\omega \sum_{i=1}^{N_b-1} [1 - \cos(\omega_i)] + k_\psi \sum_{i=1}^{N_b-1} [1 - \cos(\psi_i)], \quad (3)
\end{aligned}$$

where $\ell_i = |\mathbf{r}_{i+1} - \mathbf{r}_i|$ is the distance between adjacent sites, k_b is the bond force constant, and $\ell_{b,0}$ is the equilibrium bond length; $\cos(\beta_i) = \hat{\mathbf{r}}_{(i)(i+1)} \cdot \hat{\mathbf{r}}_{(i+1)(i+2)}$ is the angle between adjacent bonds with angle force constant k_β ; $\cos(\omega_i) = \frac{\hat{\mathbf{f}}_{i+1} \cdot \hat{\mathbf{f}}_i + \hat{\mathbf{v}}_{i+1} \cdot \hat{\mathbf{v}}_i}{(1 + \hat{\mathbf{u}}_i \cdot \hat{\mathbf{u}}_{i+1})}$ is the twist around the polymer backbone between adjacent sites and k_ω is the corresponding twist force constant. The last term, U_{align} , constrains $\hat{\mathbf{u}}_i$ of each site to be aligned with the bond vector, $\hat{\mathbf{r}}_{(i)(i+1)}$, where $\cos(\psi_i) = \hat{\mathbf{u}}_i \cdot \hat{\mathbf{r}}_{(i)(i+1)}$ and k_ψ is the corresponding force constant. Note that through k_β we can set the stiffness of the polymer.

In the following, the bonded potentials regarding polymer main backbone (PB)–spacer (SC) interactions and spacer (SC)–liquid crystal (LC) interactions have a harmonic functional form, and the difference only lies in the value of the underlying parameters. We have adopted the notation $U(\ell_{ij}; k, \ell_0) = \frac{k}{2}(\ell_{ij} - \ell_0)^2$ for the corresponding bonds, and $U(\hat{\mathbf{x}}, \hat{\mathbf{y}}; k, \theta_0) = \frac{k}{2}(\theta - \theta_0)^2$ for the corresponding angles, where $\ell_{ij} = |\mathbf{r}_{ij}|$, $\cos(\theta) = \hat{\mathbf{x}} \cdot \hat{\mathbf{y}}$, and k , ℓ_0 , and θ_0 are the corresponding force constant, equilibrium bond length, and equilibrium angle.⁶⁰

To attach the spacers to the main backbone while ensuring their syndiotacticity, we have adopted a bond potential and an orientational potential as follows

$$\begin{aligned}
U_{\text{bond}} + U_{\text{orient}} = & U_{\text{b}}(\ell_{\text{PB},i-\text{SC},j}; k_{\text{b}}^{N_{\text{SC}}}, \ell_{\text{b},0}) \\
& + U_{\text{o}}(\hat{\mathbf{r}}_{ij}, \hat{\mathbf{v}}_{\text{PB},i}; k_{\alpha}^{N_{\text{SC}}}, 90^{\circ}) + U_{\text{o}}(\hat{\mathbf{r}}_{ij}, \hat{\mathbf{v}}_{\text{SC},j}; k_{\alpha}^{N_{\text{SC}}}, 90^{\circ}) + U_{\text{o}}(\hat{\mathbf{v}}_{\text{PB},i}, \hat{\mathbf{v}}_{\text{SC},j}; k_{\alpha}^{N_{\text{SC}}}, 180^{\circ}) \\
& + U_{\text{o}}(\hat{\mathbf{r}}_{ij}, \hat{\mathbf{u}}_{\text{PB},i}; k_{\alpha}^{N_{\text{SC}}}, 90^{\circ}) + U_{\text{o}}(\hat{\mathbf{r}}_{ij}, \hat{\mathbf{u}}_{\text{SC},j}; k_{\alpha}^{N_{\text{SC}}}, 0^{\circ}) + U_{\text{o}}(\hat{\mathbf{u}}_{\text{PB},i}, \hat{\mathbf{u}}_{\text{SC},j}; k_{\alpha}^{N_{\text{SC}}}, 90^{\circ}), \quad (4)
\end{aligned}$$

where N_{SC} is the number of spacers, and the angles are the result from the dot product between the corresponding unit orientational vectors specified. From here it can be deduced that if one is interested in isotactic or atactic configurations, it would suffice to modify or eliminate the U_{orient} potential, respectively.

Finally, we have employed a bonding potential to attach the terminal mesogenic group that represents a liquid crystal unit to the spacers and torsional potentials that prevent the ellipsoids from unphysical rotations with respect to the rest of the chain and also set the liquid crystal type of attachment; end-on side-chain (EOSC) and side-on side-chain (SOSC) configurations.

For the EOSC configuration, the potential is given by

$$\begin{aligned}
U_{\text{bond}} + U_{\text{orient}} \\
= & U_{\text{b}}(\ell_{\text{SC},i-\text{LC},i+1}; k_{\text{b,EOSC}}^{N_{\text{SC}}}, \ell_{\text{b},0,\text{EOSC}}) + U_{\text{o}}(\hat{\mathbf{f}}_{\text{SC},i}, \hat{\mathbf{f}}_{\text{LC},i+1}; k_{\xi}^{N_{\text{SC}}}, 90^{\circ}) \\
& + U_{\text{o}}(\hat{\mathbf{r}}_{(i)(i+1)}, \hat{\mathbf{u}}_{\text{SC},i}; k_{\xi}^{N_{\text{SC}}}, 0^{\circ}) + U_{\text{o}}(\hat{\mathbf{r}}_{(i)(i+1)}, \hat{\mathbf{u}}_{\text{LC},i+1}; k_{\xi}^{N_{\text{SC}}}, 0^{\circ}). \quad (5)
\end{aligned}$$

and for the SOSC configuration, the potential is given by

$$U_{\text{bond}} + U_{\text{orient}}$$

$$= U_b(\ell_{\text{SC},i-\text{LC},i+1}; k_{\text{b,SOSC}}^{N_{\text{SC}}}, \ell_{\text{b},0,\text{SOSC}}) + U_o(\hat{v}_{\text{SC},i}, \hat{v}_{\text{LC},i+1}; k_{\xi}^{N_{\text{SC}}}, 180^\circ) \\ + U_o(\hat{r}_{(i)(i+1)}, \hat{u}_{\text{SC},i}; k_{\xi}^{N_{\text{SC}}}, 0^\circ) + U_o(\hat{r}_{(i)(i+1)}, \hat{u}_{\text{LC},i+1}; k_{\xi}^{N_{\text{SC}}}, 90^\circ), \quad (6)$$

Quaternion-based methods for time integration of anisotropic sites and thermostatting/barostatting of their rotational degrees of freedom are taken into account in this work. All the parameter values used for U_{bonded} are given in the supplementary material.

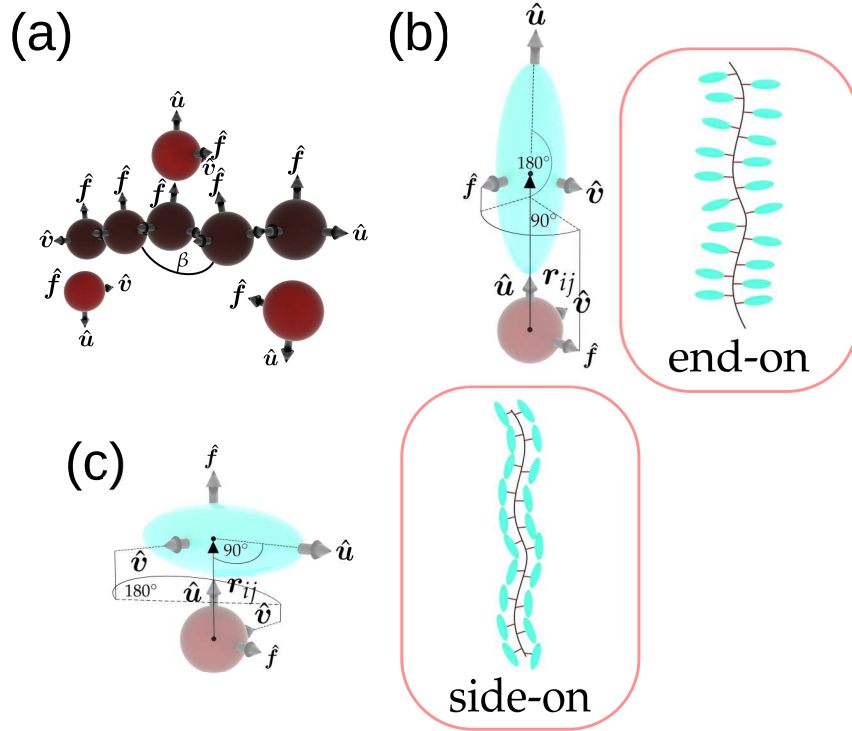


Figure 2: (a) Bonded interactions for the polymer backbone (dark scarlet) and some spacer beads (scarlet) attached to it. Here, β represents the bending angle between three adjacent atoms and the \hat{f} , \hat{v} , \hat{u} unit vectors (arrows) denote the orientation of each anisotropic site. (b) Bonded interactions between the mesogenic unit (cyan ellipsoid) attached in an end-on manner to a spacer bead (scarlet). (c) Bonded interactions between the mesogenic unit (cyan ellipsoid) attached in a side-on manner to a spacer bead (scarlet).

Simulation methodology

The SCLCP molecules are grown from random positions inside the computational box by treating each molecule as a 3D random walk. The resultant configuration consists of overlapping SCLCP molecules. The MD simulations are performed using the open-source LAMMPS package.⁶¹ The equations of motion are propagated via the velocity-Verlet algorithm with a time step of 0.002τ , where $\tau = \sigma \sqrt{m/\epsilon}$. Periodic boundary conditions are applied in all three uncoupled dimensions of the box. The first equilibration steps are performed with a soft repulsive potential (slow push-off method) which allows SCLCPs to pass through each other, introducing excluded volume interactions incrementally. After equilibrating the melt with the slow push-off method, systems are equilibrated in the isothermal-isobaric (NPT) ensemble using a Langevin thermostat and a Berendsen barostat with the full potentials for at least 3 times the longest end-to-end vector relaxation time at a temperature $T = 8.0 \epsilon/k_B$ and pressure $P = 1.0 \epsilon/\sigma^3$ (see Subsec.) to obtain an isotropic melt with no memory of the initial spatial arrangement. The damping parameters for the thermostat and barostat are set to 0.5τ and 5τ , respectively.

To study mesophase behavior, we gradually cool down the systems from equilibrated isotropic melts at $T = 8.0 \epsilon/k_B$ and $P = 1.0 \epsilon/\sigma^3$ until crystalline order is reached as explained below.

In this work, we study polymers with purely end-on and purely side-on LC groups separately. We consider different variations of architectural parameters of the SCLCP model, namely; two backbone lengths, three spacer lengths, and three polymer stiffnesses (this is controlled by the angle force constant, k_β). This gives rise to 12 different systems where the total number of particles is kept constant for all simulated cases. Here, the notation employed for the systems is as follows [A:B:C], where A is the number of backbone beads, B is the number of spacer beads, and C is the angle force constant in dimensionless units. Table 1 shows every case simulated in this work. Note that only for comparison purposes we have also simulated a melt of linear polymer chains [100:0:1.5] without LC

units attached.

The mean properties are represented by statistical averages over all of the SCLCPs of the system configurations evenly taken from the last steps of a particular simulation.

Table 1: Side-chain liquid crystal polymer systems studied with their corresponding notation that reflects their architectural properties. Each system is replicated and studied for both end-on side-chain (EOSC) and side-on side-chain (SOSC) liquid crystal polymers.

| System | Number of SCLCP molecules (N_m) | Number of particles (N_p) |
|-------------|-------------------------------------|-------------------------------|
| [44:6:1.5] | 636 | 125,928 |
| [100:2:1.5] | 504 | 126,000 |
| [100:4:1.5] | 360 | 126,000 |
| [100:6:0.0] | 280 | 126,000 |
| [100:6:1.5] | 280 | 126,000 |
| [100:6:5.0] | 280 | 126,000 |

Cooling simulations

Here, a cooling rate of $5 \times 10^{-5} (\epsilon/k_B)/\tau$ is employed. The studied temperatures are: 8.0, 7.0, 6.0, 5.0, 4.0, 3.0, 2.5, 2.0, 1.5, and 1.0. From the starting relaxed isotropic configuration of each system at $T = 8.0 \epsilon/k_B$ and $P = 1.0 \epsilon/\sigma^3$, the samples are cooled using the specified cooling rate in NVT ensemble, and at each temperature studied the system is relaxed in NPT ensemble at $P = 1.0 \epsilon/\sigma^3$ during $4,000 \tau$. The natural evolution of these systems is to display local ordering of the liquid crystals as the temperature decreases. To obtain global and positional ordering of the LC layers one could apply an external alignment field that induces a preferential orientation of LC molecules as explained below. Therefore, we apply this external field to the main axis of LC moieties in a particular direction during the cooling simulations. This alignment field is switched off in the relaxation simulations at the specific studied temperatures. When the field is switched off at high temperatures, the global ordering vanishes, but this changes when moving to lower temperatures, where the structure acquires global and positional ordering.

External alignment field

To induce artificial alignment of liquid crystals with global ordering and to avoid the long simulation times required for mesophase formation, we have implemented an external alignment field in LAMMPS⁶¹ that applies a torque to the orientation of a particle, in this particular case, to the main axis of the uniaxial ellipsoids representing liquid crystals with respect to a fixed axial direction.

This external torque applied to the molecules mimics an external magnetic field applied to liquid crystals, which are employed in experiments, to align them parallel to the field, thus obtaining global ordering.¹⁷ Similar potentials used in previous works^{27,51} have shown that both the external field and its strength affect the structures formed in the microphase.

In particular, the applied torque is as follows

$$\boldsymbol{\tau}_{\text{align}} = \begin{cases} k_{\text{align}} \hat{\mathbf{u}}_i \times \hat{\mathbf{e}} & \text{if } \hat{\mathbf{u}}_i \cdot \hat{\mathbf{e}} > 0 \\ -k_{\text{align}} \hat{\mathbf{u}}_i \times \hat{\mathbf{e}} & \text{if } \hat{\mathbf{u}}_i \cdot \hat{\mathbf{e}} < 0 \end{cases} \quad (7)$$

where k_{align} is the force constant that determines how aggressive is the external alignment field, and $\hat{\mathbf{e}}$ is the unit directional vector. The direction of $\hat{\mathbf{e}}$ can be set in any direction of a fixed 3D space. This torque allows us for a parallel alignment of the LC moieties with respect to the field, regardless of whether their main axis ($\hat{\mathbf{u}}_i$) is pointing in the opposite direction as $\hat{\mathbf{e}}$. Here, k_{align} is set to $45 k_{\text{B}}T$.

RESULTS AND DISCUSSION

Equilibration of the systems

We calculate chain observables and examine their dependence on architectural parameters. All the measurements are performed on melt systems after the equilibration process at $T = 8.0 \varepsilon/k_B$ and $P = 1.0 \varepsilon/\sigma^3$. Firstly, we analyze the backbone's end-to-end vector relaxation. Specifically, we calculate the end-to-end vector autocorrelation function (ACF_{ee}) defined as $\frac{\langle \mathbf{R}_{ee}(t) \cdot \mathbf{R}_{ee}(0) \rangle}{\langle R_{ee}^2 \rangle}$, where \mathbf{R}_{ee} is the vector from the first backbone bead to the last backbone bead. The function was calculated for time blocks of $30,000 \tau$ with starting times spaced $2,000 \tau$ apart. These block-averaged functions were then averaged over 15 trials with different starting configurations of the SCLCP melt systems. Figure 3a shows the mean backbone's end-to-end vector relaxation time for the systems with different backbone lengths, spacer lengths, angle force constants, and mesogenic types of attachment (end-on and side-on configurations). To ensure proper relaxation of SCLCP systems, equilibration times are at least 3 times the longest end-to-end vector relaxation time (the intersection at $1/e$). Comparing the SCLCP systems with the linear polymer melt system, we found that the presence of side chains (spacers and LC moieties) slows down the relaxation of the former by one order of magnitude on average, as would be intuitively expected. Specifically, for SCLCP systems, the end-to-end vector relaxation time is found to be dependent on the backbone length and spacer length. This effect is expected due to the presence of polymer entanglements in systems composed of long polymer chains, even when our systems should be only slightly entangled for chains composed of 100 beads. Our results also show that the mesogen type of attachment and angle force constant (k_β) have a minimal or no effect on the end-to-end autocorrelation time, at least for the angle force constants studied here since it is well studied that entanglement properties vary with chain stiffness.⁷⁵

Secondly, for the mean-squared internal distance curves shown in Figure 3b, each

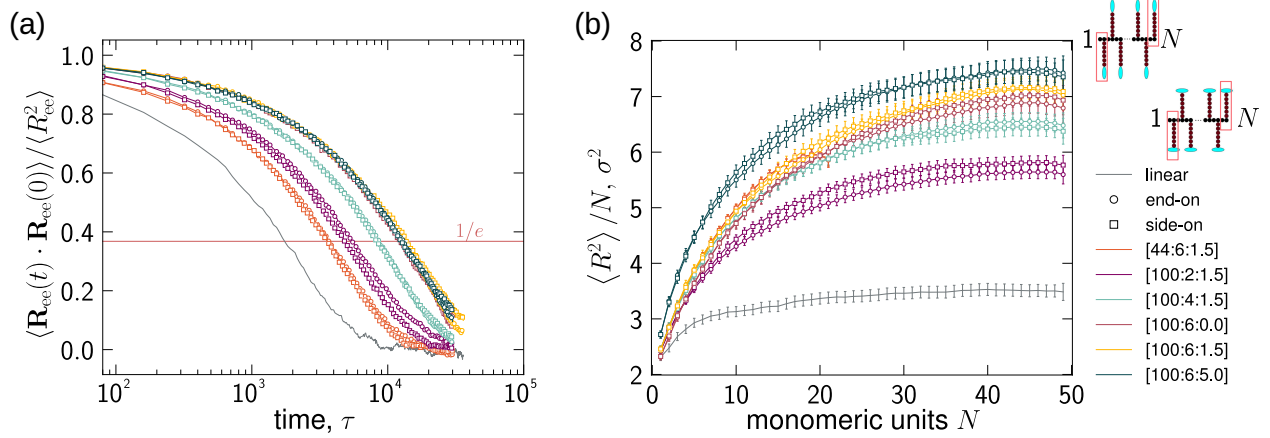


Figure 3: (a) End-to-end vector autocorrelation function (ACF_{ee}) for all the melt systems studied. (b) Mean-squared internal distances $\langle R^2 \rangle / N$ as a function of monomeric units N for all the equilibrated melt systems at $T = 8.0 \epsilon / k_B$ and $P = 1.0 \epsilon / \sigma^3$. Simulations for end-on side-chain (EOSC) and side-on side-chain (SOSC) configurations are shown for each case with different architectural parameters. Results for a linear polymer melt modeled with the same SCLCP backbone potential are included for comparison in (a) and (b). Schemes of how monomeric units are defined in SCLCP molecules are depicted in (b).

$\langle R^2 \rangle / N$ point (with N the number of monomeric units), where a monomer in the SCLCP model is defined as two consecutive backbone beads and the corresponding side chain that is attached to one of them, is calculated by averaging over all of the chains of 10 melt configurations, spaced 9,000 τ from each other and from the last 90,000 τ of simulation. In all cases, a plateau in the $\langle R^2 \rangle / N$ vs N curve is obtained. The mean-squared internal distances are strictly correlated to chain structure and have shown to be non-dependent on the mesogenic type of attachment. It can be observed that within the statistical error bars (standard error), there are no significant differences between EOSC and SOSC configurations. On the other hand, the $\langle R^2 \rangle / N$ observable is strongly dependent on the spacer length, due to steric effects, and on the angle force constant, being greater for higher values of k_β , which is intuitive since one would expect stiffer chains to be more elongated. Finally, a trend can be observed for different backbone lengths, specifically if one compares between [44:6:1.5] and [100:6:1.5] cases. Here, for linear polymer chains of a particular chemistry, the value of the plateau should be the same for the same tem-

perature regardless of backbone length (if normalized by molecular weight), however, for SCLCP molecules, having longer backbone chains means more side chains attached, which induces a higher excluded volume due to the steric effect, and these are more effective at keeping other chains away.⁷⁵ This effect can be easily observed also if one compares the different plateau values for the [100:6:1.5] and the melt composed of linear polymer chains [100:0:1.5] that share the same number of backbone beads.

Structure of mesophases

After corroborating equilibration and relaxation at high temperatures, we next proceed to investigate the structure of mesophases at different thermodynamic states. In doing that, we slowly cool down the systems to lower temperatures, while, as explained above, an external alignment field is applied intermittently during the cooling process to ensure alignment occurs in a given direction, avoiding multiple crystalline domains with different orientations.

Through system visualizations using the software OVITO,⁷⁶ we corroborate that SCLCP systems with only one type of LC moiety indeed form well-organized structures at low temperatures, as shown in Figure 4 that remain stable even after the alignment field is switched off.

Interestingly, as can be seen in Figure 4 for [100:6:1.5] systems, at low temperatures, purely end-on and side-on systems give rise to different morphologies. Figure 4a shows top and front views of the mesophases formed for the EOSC [100:6:1.5] system at 3 different temperatures from equilibrium runs (here, the external alignment field is switched off): at $T = 8.0 \epsilon/k_B$, the structure is completely isotropic without any kind of global or local ordering; at $T = 2.5 \epsilon/k_B$, it is not possible to appreciate a global ordering of the mesogens but a local ordering can be observed, and also an elongation of the system in the direction perpendicular to which the alignment field is applied during cooling simulations; at $T = 1.0 \epsilon/k_B$, it can be seen how the system slightly shrinks in the elongated

direction due to decreased temperature (see Figure 4a, middle and right snapshots), and a global ordering can be observed. In particular, from the front view, it can be observed that liquid crystals, polymer backbones, and the spacers all display a global ordering, with the mesogens arranged in a bilayer (smectic B-like mesophase). Also, from the snapshot at $T = 1.0 \varepsilon/k_B$ we can conclude that the elongation is favored in the direction parallel to the polymer backbones, thus perpendicular to the LC director, in line with experimental results.⁸ Moreover, the LC bilayer is slightly tilted, and some defects can be appreciated as in real networks^{77,78} and previous MD simulations.⁵¹ From the top view at low temperatures, the LCs adopt a hexagonal lattice, which indicates crystalline order. The smectic B-like phase displayed by end-on side-chain systems at low temperatures is in good agreement with what was found in previous works for smaller systems.^{27,51} On the other hand, a similar behavior can be observed for side-on side-chain systems at high temperatures, that is, isotropic ordering without preferential alignment. However, unlike EOSC systems, at low temperatures the SOSC systems exhibit nematic ordering in one direction due to how the LCs are attached to the spacer, as shown in the front view of Figure 4b. In the top view of Figure 4b, it can be seen that LCs surround the polymer backbones. In this way, a remarkably hexagonal structure is formed, which is possibly the most energetically stable configuration in this thermodynamic state. The elongation of the system, in this case, is also in the direction perpendicular to the LC director but much less pronounced than in the EOSC case.

Snapshots that include all studied systems with different variations of the architectural parameters are shown in the supplementary material. Among the most notable variations, we find that for systems with short spacers ([100:2:1.5]), very high elongations occur in different directions depending on the LC configurations (either end-on or side-on), which we relate to the great coupling between LCs and the polymer backbones. Regarding polymer stiffness, we find that the most flexible polymer (EOSC [100:6:0.0] system) forms a very well-ordered smectic B-like structure, where three LC bilayers can

be observed inside the box and the same high ordering in a hexagonal structure for SOSC [100:6:0.0] systems; while the stiffest polymer systems in the EOSC [100:6:5.0] configuration shows only monolayers of LC units and a more elongated structure in the opposite direction of the LC director as expected and for the SOSC [100:6:5.0] configuration the ordering at low temperatures is not so remarkable.

We calculate the mean-square radius of gyration of the polymer backbone for all the systems studied at different temperatures. As shown in Figure 5 the $\langle R_g^2 \rangle$ decreases for all the systems as the temperature decreases and reaches a plateau for the crystalline order at low temperatures. If LC types of attachments are compared (left side against the right side in Figure 5) we observe only a slight difference between end-on and side-on configurations. In some cases, at low temperatures, the end-on configurations display higher values than side-on configurations.

SCLCP systems with different backbones lengths are compared and as expected the [100:6:1.5] systems (with longer backbones) display higher values than the [44:6:1.5] system. By varying the spacer length, a clear trend can be observed in Figures 5a,b; at high temperatures, due to a steric effect, the $\langle R_g^2 \rangle$ is larger for longer spacers. This trend is maintained throughout the entire temperature range, the only exception is the EOSC [100:2:1.5] at low temperatures, which again could be due to an artifact for the [100:2:1.5] systems at low temperatures. On the other hand, Figures 5c,d show a greater mean square radius of gyration for the stiffest polymer chain, which even at low temperatures holds a similar value to those displayed at high temperatures for both end-on and side-on configurations.

We also calculate the anisotropic ratio defined as $\sqrt{\langle R_{ee\parallel}^2 \rangle / \langle R_{ee\perp}^2 \rangle}$, where $\langle R_{ee\parallel}^2 \rangle$ is the mean square end-to-end distance vector in the direction parallel to the alignment field, and $\langle R_{ee\perp}^2 \rangle$ is the mean square end-to-end distance in the perpendicular direction to the alignment field.

Wang and Wang⁴⁴ employed this parameter to characterize their model for SCLCPs.

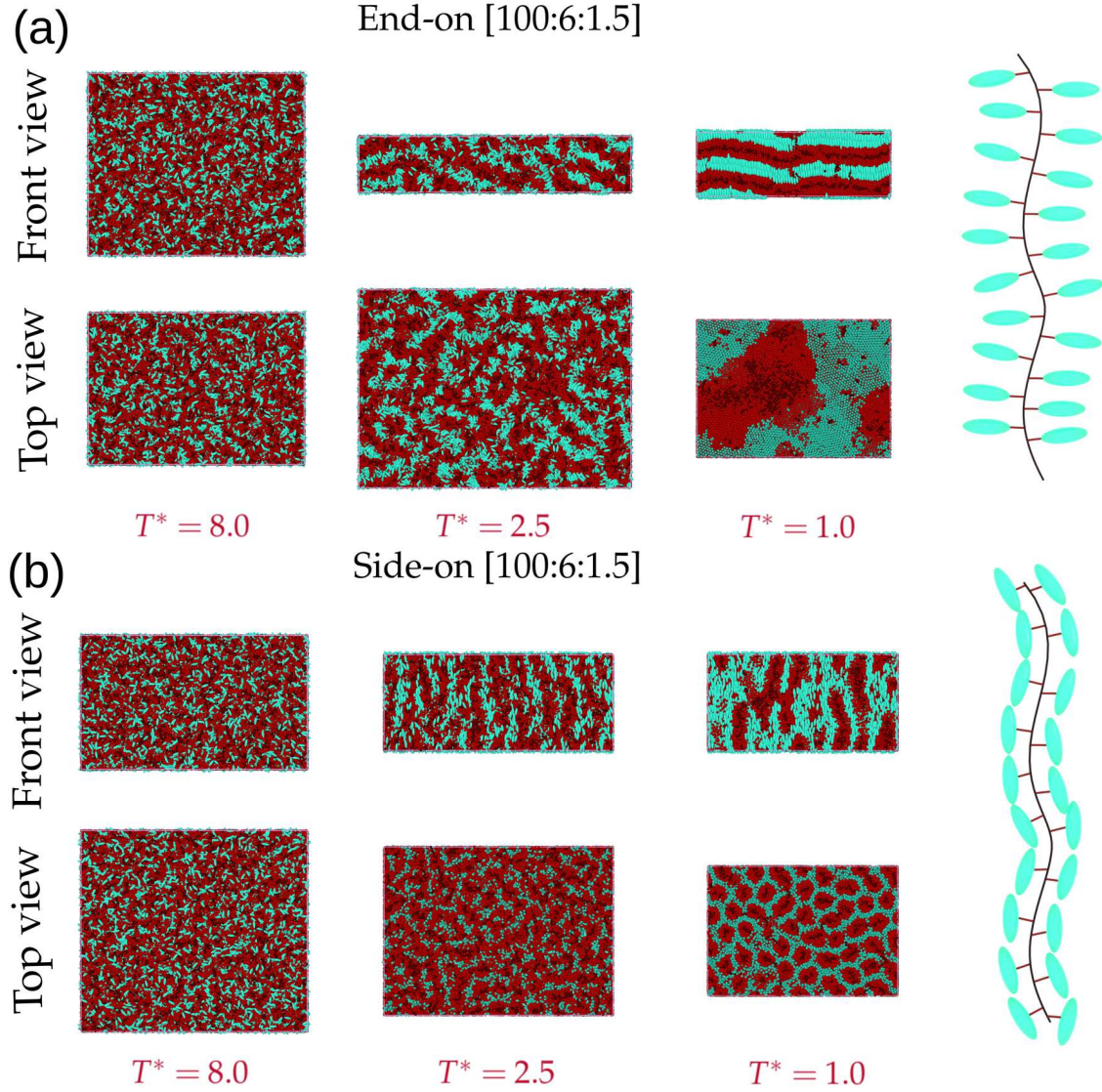


Figure 4: Snapshots of SCLCP [100:6:1.5] systems (top and front views) from equilibrium simulations at different thermodynamic states for (a) end-on side-chain (EOSC) configuration and (b) side-on side-chain (SOSC) configuration. From left to right, mesophases from isotropic to crystalline order can be observed, where cyan represents liquid crystals, scarlet represents spacers, and dark scarlet represents polymer backbones.

They modeled the interaction between the polymer backbone and the LC side groups through two coupling effects: the global nematic coupling and the local hinge effect. The global coupling involves the interaction of a backbone segment with the average nematic field produced by all LC side groups in its vicinity whereas the hinge effect involves the instantaneous values of the orientation vectors of the chain segment and its own attached LC side group, which is purely an intrachain effect.⁴⁴ Moreover, they neglected the volume occupied by the spacer in their model, but its effect in terms of interactions is implicitly included. The base case that they employed consisted of one side chain per Kuhn segment, but more graft densities are explored. They found a value higher than 1 for all the cases studied for the side-on configurations, which means a prolate conformation. By decreasing grafting density, the anisotropic ratio decreased (becoming less prolate), but remained higher than 1. On the other hand, the conformation for the end-on SCLCPs displayed both oblate and prolate conformations depending on the graft density, since the two coupling effects are reported to be competitive in that case. Therefore for the base case, they obtained values smaller than 1 for the anisotropic ratio $\sqrt{\langle R_{ee\parallel}^2 \rangle / \langle R_{ee\perp}^2 \rangle}$ which means oblate conformations ($\langle R_{ee\perp}^2 \rangle > \langle R_{ee\parallel}^2 \rangle$), but for decreased grafting density values higher than 1 were displayed.

Figure 5 shows the anisotropic ratio $\sqrt{\langle R_{ee\parallel}^2 \rangle / \langle R_{ee\perp}^2 \rangle}$ the systems studied. From $T = 8\varepsilon/k_B$ to $T = 4\varepsilon/k_B$ is safe to say that all the systems display the isotropic value of one with the only exception of the [100:2:1.5] systems due to the higher LC-backbone coupling. That means even at high temperatures the EOSC [100:2:1.5] (Figure 5a) display oblate conformation (anisotropic ratio smaller than 1) and the SOSC [100:2:1.5] (Figure 5b) display prolate conformation (anisotropic ratio higher than 1). At lower temperatures, these two systems completely change their conformation, which may be due to simulation artifacts or probably some molecular effects in the crystalline regime. If we compare Figure 5c,d where different chain stiffness are studied for end-on and side-on configurations, respectively, two clear trends can be observed; (i) the anisotropic ratio of the end-on

SCLCP systems tends to decrease at temperatures lower than $4\varepsilon/k_B$ up to $T = 2.5\varepsilon/k_B$ close to the isotropic to liquid crystal transition. In this range the anisotropic ratio adopts values smaller than 1, therefore the chains adopt an oblate conformation in agreement with the theoretical model of Wang and Wang⁴⁴ and experimental results.⁸ At temperatures lower than $2.5\varepsilon/k_B$, in the crystalline regime the anisotropic parameter display values higher than 1, which means that the chains adopt a prolate conformation. We infer that this effect could be to some molecular coupling at very low temperatures. The same trend is followed for the EOSC [100:4:1.5]. (ii) The anisotropic ratio of the side-in SCLCP systems tends to hold the isotropic value of 1 up to $T = 2\varepsilon/k_B$ since the transition temperatures are lower for these systems when compared with the end-on side-chain systems. At lower temperatures in the crystalline regime, the anisotropic ratio tends to adopt values higher than 1, therefore the chains display prolate conformations (see Figures 5c,d) in agreement with experimental results⁸ and theory.⁴⁴ The SOSC [100:6:5.0] system represents an exception here along with the SOSC [100:2:1.5] system. The former could be due to the stiffness affecting the rotational coupling between the spherical and aspherical beads of the model.

Orientational order parameter

To quantify the overall degree of molecular ordering, an instantaneous alignment second-rank tensor is defined as

$$Q_{\alpha\beta} = \frac{1}{N_{LC}} \sum_{i=1}^{N_{LC}} \frac{3}{2} \left[(\hat{\mathbf{u}}_i)_\alpha (\hat{\mathbf{u}}_i)_\beta - \frac{1}{3} \delta_{\alpha\beta} \right], \quad (8)$$

where N_{LC} is the number of LC units in the system, $\delta_{\alpha\beta}$ is the Kronecker delta function, and $(\hat{\mathbf{u}}_i)_\alpha$ are the Cartesian coordinates ($\alpha = x, y, z$) of the main axis of the i th mesogen ($i = 1, 2, \dots, N_{LC}$) (see reference⁷⁹ for more details on this calculation). The time average of the largest eigenvalue of the alignment tensor $Q_{\alpha\beta}$ is equal to the orientational order parameter S_2 (which is in fact the second-order Legendre polynomial, $P_2(\cos \theta_m)$, where

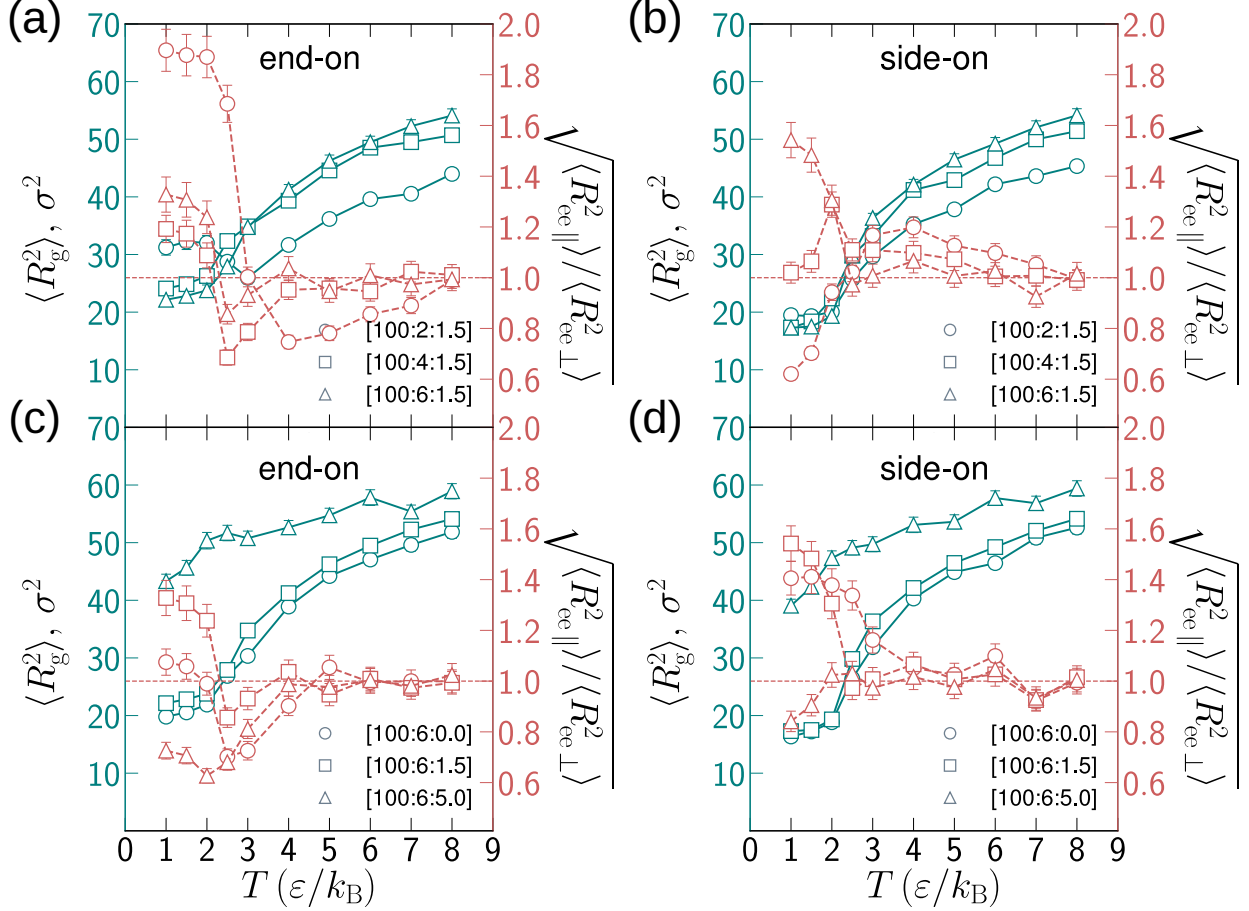


Figure 5: Mean-square radius of gyration of the backbone $\langle R_g^2 \rangle$ (turquoise and continuous lines) and the anisotropic ratio $\sqrt{\langle R_{ee\parallel}^2 \rangle / \langle R_{ee\perp}^2 \rangle}$ (red and dashed lines) for different systems at different temperatures from equilibrium simulations. The standard errors are propagated in the latter and included in all the measurements. The effect of architecture parameters on $\langle R_g^2 \rangle$ and $\sqrt{\langle R_{ee\parallel}^2 \rangle / \langle R_{ee\perp}^2 \rangle}$ as a function of temperature is shown for different spacer lengths in a) for end-on side-chain (EOSC) configurations and in b) for side-on side-chain (SOSC) configurations, and for different angle force constants (k_β) in c) for end-on side-chain (EOSC) configurations and in d) for side-on side-chain (SOSC) configurations. The isotropic value (1) for $\sqrt{\langle R_{ee\parallel}^2 \rangle / \langle R_{ee\perp}^2 \rangle}$ is depicted in red as a guide for the eye.

θ_m is the angle between a LC particle and the LC director) and the associated eigenvector gives the macroscopic director \hat{n} . A value of $S_2 = 0$ corresponds to a non-oriented isotropic phase, while $S_2 = 1$ to a perfectly aligned mesophase.

Figure 6 shows the global order parameter S_2 for EOSC and SOSC systems as labeled, where different variations of architectural parameters are presented. S_2 values are shown for relaxation simulations at specific temperatures (where the external alignment field is switched off) and for cooling simulations (where the external alignment field is switched on) throughout the process (see Subsec. for more details). At high temperatures ($T > 3\epsilon/k_B$), the global order parameter, S_2 , linearly increases as the temperature decreases during the cooling runs when the external alignment field is switched on. Here, S_2 values are similar for all cases. However, when the system is relaxed at a specific temperature (after the alignment field is switched off), S_2 decays to zero as the system returns to its global isotropic order. This can be observed in all the different cases studied. On the other hand, at lower temperatures, S_2 starts to increase and crystalline order is reached. For all the cases, the liquid crystal to isotropic transition temperatures (T_{LC-I}) of EOSC systems are consistently higher than those of SOSC systems. We believe that the reason behind this trend is that configurational assembly is more favorable for end-on side-chain systems than those for side-on side-chain systems when the different LC moieties are identically modeled by the same type of ellipsoidal bead since for end-on LC configuration, the mesogenic unit acts more like an extension of the spacer they are attached to. In experiments,⁸ the values of the T_{LC-I} may vary depending on the liquid crystal chemistry employed, being also possible higher temperatures for side-on side-chain systems. The reproducibility of specific transition temperatures is outside the scope of this work, but we believe that it can be implemented by varying the model parameters.

Some specific architectural trends that can be observed in global ordering are: (i) SCLCP systems with shorter backbone lengths display higher T_{LC-I} , or similarly the parameter S_2 increases its value earlier when the system is cooled down. This is valid for

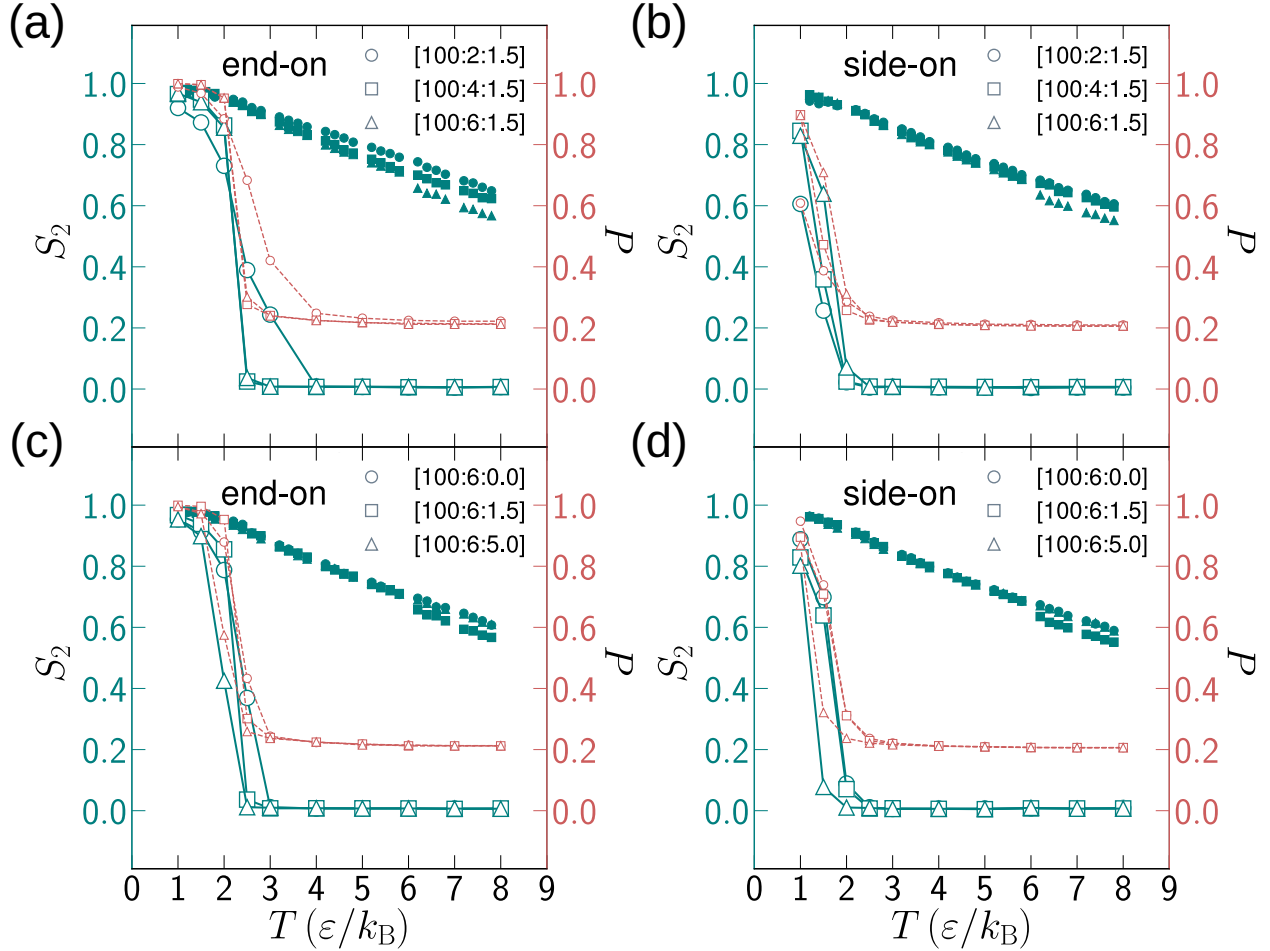


Figure 6: Global orientational order parameter S_2 (turquoise and continuous lines) for different systems as labeled at different temperatures from equilibrium simulations (empty symbols) after the alignment field is switched off and from cooling runs (filled symbols) when the alignment field is switched on. The effect of architecture parameters on S_2 as a function of temperature is shown for different spacer lengths in a) for end-on side-chain (EOSC) configurations and in b) for side-on side-chain (SOSC) configurations, and for different angle force constants (k_β) in c) for end-on side-chain (EOSC) configurations and in d) for side-on side-chain (SOSC) configurations. Error bars are smaller than the symbols. The probability of local orientational order is also shown (red and dashed lines) at different temperatures.

both end-on and side-on configurations, probably because of fewer steric impediments. (ii) For systems with different spacer lengths (Figures 6a,b), we observe that the SCLCP system with the shortest side chain crystallizes much earlier for the EOSC configuration. The opposite is observed for the SOSC configuration. These trends are maintained as the number of spacer beads increases. We infer that in the particular case of systems with spacers composed of 2 beads, they do not encounter as many steric hindrances as long side chains, but at the same time, the polymer backbone and the mesogen are very coupled, and for the side-on configuration, the intramolecular interaction between the polymer and the LC could be unfavorable for this particular case. Furthermore, for both [100:2:1.5] cases, the system is highly elongated, which can be generated by this unfavorable tradeoff. Finally, (iii) regarding different polymer stiffnesses (Figures 6c,d), the most flexible polymer ($k_\beta = 0.0 k_B T$) is the one with the highest T_{LC-I} for both end-on and side-on configurations, this is due to the low coupling between the polymer backbone and the LC moieties so that the latter can interact with the rest of the LCs in the system without major restrictions. On the contrary, stiffer systems show lower transition temperatures.

Since LC clustering can appear even when global ordering is ~ 0 , we quantify local ordering by defining P as the probability of finding neighbor mesogens with $|\hat{\mathbf{u}}_i \cdot \hat{\mathbf{u}}_j| > 0.8$ where $\hat{\mathbf{u}}_i$ and $\hat{\mathbf{u}}_j$ are the unit vectors of the main axis of two LCs within a distance less than 3.4σ . P follows the same S_2 trend for both end-on and side-on configurations but shows a higher value, especially at higher temperatures where local but not long-range order is present.

We have also performed two separate tests for the EOSC [100:6:1.5] system. The first test consisted of cooling this particular system from its high-temperature thermodynamic state with isotropic structure, where no external alignment field is applied and the same cooling rate is employed in the NPT ensemble. The structure at $T = 2.0 \varepsilon/k_B$ and $P = 1.0 \varepsilon/\sigma^3$ is shown in Figure 7a. Here, polysmectic domains are formed, with highly local but not global ordering. In particular, at $T = 2 \varepsilon/k_B$, the calculated S_2 is

≈ 0.16 and the calculated P is ≈ 0.84 . In Stimson and Wilson²⁷ it is said that without an external alignment field the system will evolve in the same globally ordered structure but longer timescales are needed, which are unreachable for MD simulations. Based on our results, we think that without an external alignment field there is no specific director vector induced and the system will form layers that over time will form constraints at low temperatures in different directions creating entropically trapped systems that will remain in a polysmectic mesophase.

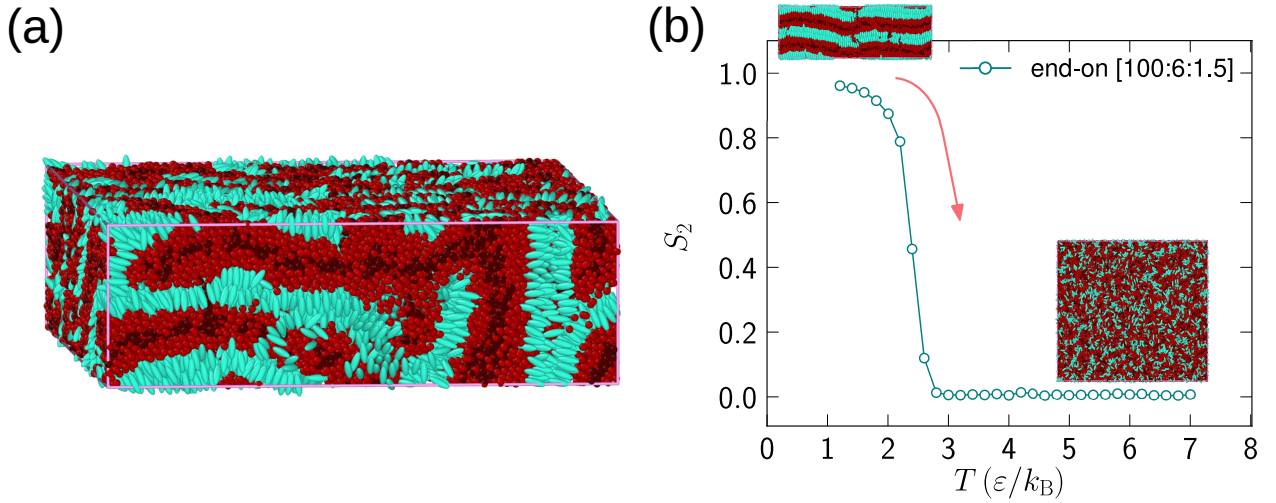


Figure 7: (a) End-on SCLCP [100:6:1.5] configuration at $T = 2.0 \epsilon/k_B$ and $P = 1.0 \epsilon/\sigma^3$ resulting from a cooling run from isotropic state ($T = 8.0 \epsilon/k_B$ and $P = 1.0 \epsilon/\sigma^3$) without applying the external alignment field to the LC particles. (b) Global orientational order parameter S_2 for the end-on SCLCP [100:6:1.5] configuration at different temperatures resulting from heating the system from smectic B-like to isotropic mesophase without applying the external alignment field. A red arrow is depicted to illustrate the direction of the process.

In the second test, we started from the configuration at $T = 1.0 \epsilon/k_B$ and $P = 1.0 \epsilon/\sigma^3$, which reached that state after applying the procedure explained in Subsec. , and we bring it to a thermodynamic state at $T = 7.0 \epsilon/k_B$ and $P = 1.0 \epsilon/\sigma^3$ by increasing the temperature at a rate of $5 \times 10^{-5} (\epsilon/k_B)/\tau$ without applying the external alignment field at any point of the simulation. In Figure 7b it is shown that the system returns to a completely isotropic state at high temperatures, and that the S_2 curve displayed is very similar to that of Figure 6c.

Radial distribution function

We have also calculated the radial distribution function for the liquid crystals, $g_{\text{LC-LC}}(r)$, at different temperatures for all systems studied in alignment field-free equilibrium state. Specifically, $g_{\text{LC-LC}}(r)$ is calculated in the standard way, as the average number of times a LC unit would observe another LC a distance between r and $r + \Delta r$ from itself, normalized by the expected number at uniform density (i.e., the number of other LCs in the system divided by the system volume). The range of $g_{\text{LC-LC}}(r)$ is from 0 to large positive numbers. It equals 1 indicates random distribution, a larger value for enrichment, and less than 1 for depletion of mesogens at a given separation range.

In Figure 8, we show the $g_{\text{LC-LC}}(r)$ for end-on configuration systems at different temperatures and for different architectural parameters. At high temperatures, the curves look the same, without peaks due to the isotropic regime of the systems in this thermodynamic state. Overall, if we focus on the first (nearest neighbor) peak for every system, we can see that this appears at $\sim 2.25\sigma$ for temperatures below $2.5\epsilon/k_B$ for all the systems. At $T = 1.0\epsilon/k_B$ we find the highest peak corresponding to the greatest LC packing. The second peak is split in the middle which is characteristic of hexagonal lattice arrangement as is shown in the top view of Figure 4a at low temperature. Finally, in most cases at low temperatures, an undulation extending along the computational box can be observed, this reflects and confirms the lamellar smectic B-like order in the end-on side-chain systems.

Particularly, if the cases for different backbone lengths are compared, it can be observed that they are very similar to each other in structural terms. Now, if we compare cases with different spacer lengths (Figure 8a,b,c), it can be observed that the first peak increases as this architectural parameter increases, this implies that the greater the LC-backbone decoupling, the greater the ordering and packing of the mesogens. It can also be observed that the particular case of EOSC [100:2:1.5] (Figure 8a), presents neither the division of the second peak split corresponding to hexagonal order nor undulation at long distances, which is due to the high elongation of the system and its high $T_{\text{LC-I}}$

which could cause probable artifacts in the results. For different polymer stiffnesses (Figure 8d,e,f), the higher the polymer stiffness, the higher the first peak at low temperatures but at the same time a noisier long-distance undulation because the smectic B-like order formed at low temperatures for EOSC [100:6: 5.0] (Figure 8f), is only composed of a monolayer and not of a bilayer of LC moieties.

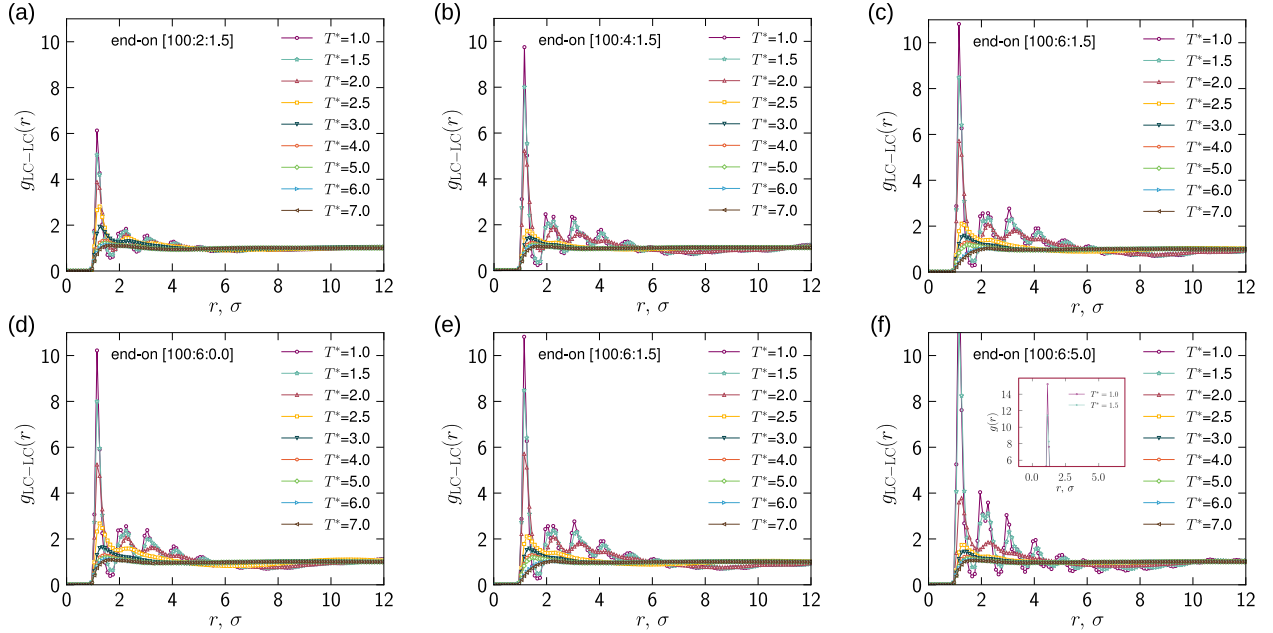


Figure 8: Liquid crystal radial distribution function $g_{LC-LC}(r)$ for all the systems studied at different temperatures from equilibrium simulations. Each subplot shows the values only for end-on side-chain (EOSC) configuration. The effect of architecture parameters on $g_{LC-LC}(r)$ as a function of temperature is shown in (a, b, c) for different spacer lengths, and in (d, e, f) for different angle force constants (k_β).

All plots for the side-on SCLCP systems have similar shapes as shown in Figure 9, with peaks and local maxima forming at temperatures lower than the crystalline mesophase transition temperature. If compared with EOSC systems, the first and second peaks are much smaller for SOSC cases due to the absence of smectic order. Also, patterns indicative of a hexagonal lattice arrangement along planes orthogonal to the layering direction exhibited in EOSC systems (second peak splits in the g_{LC-LC}) are no longer displayed here. The undulations showed at low temperatures for long distances are a result of the hexagonal-like shape caused by the LC moieties surrounding and isolating the polymer

chains. In both the end-on and side-on configurations, the [100:6:5.0] case demonstrated the most prominent peaks and the [100:2:1.5] case exhibited the least prominent peaks, the latter being probably resultant of artifacts in the measurements due to the high elongation of the computational box.

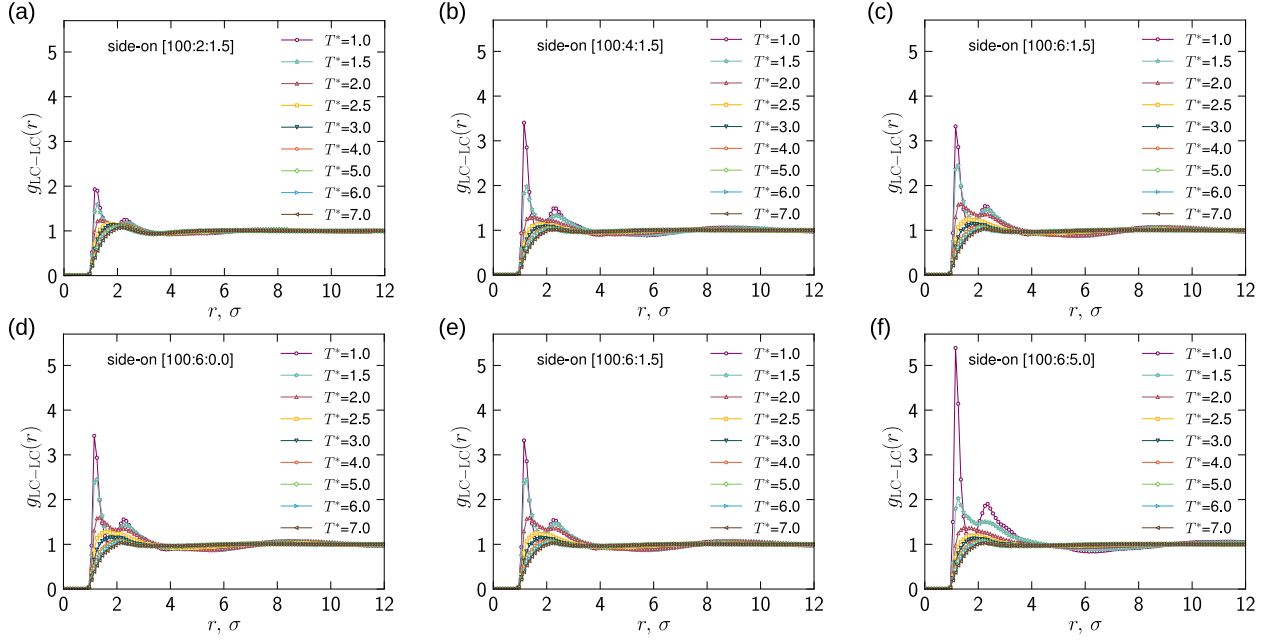


Figure 9: Liquid crystal radial distribution function $g_{\text{LC-LC}}(r)$ for all the systems studied at different temperatures from equilibrium simulations. Each subplot shows the values only for side-on side-chain (SOSC) configuration. The effect of architecture parameters on $g_{\text{LC-LC}}(r)$ as a function of temperature is shown in (a, b, c) for different spacer lengths, and in (d, e, f) for different angle force constants (k_β).

PERFORMANCE

We have measured the computational performance of the coarse-grained SCLCP model. To do this, we have made different comparisons in terms of architectural parameters. In Table 2, the first comparison is between two melts of linear polymer chains modeled in different ways. The first system modeled with the worm-like chain model, like the rest of the systems in this work, is $\sim 24\%$ less efficient than a melt composed of the same number of linear polymeric chains but modeled using the Kremer–Grest (KG) model.⁸⁰

This result confirms what was expected, a model with more degrees of freedom will be more expensive in computational terms, but $\sim 24\%$ is feasible taking into account the advantages of greater control over the system. Note that a time step of 0.002τ was used in both simulations, although generally the time step for the KG model where the beads are connected along the chain via the finitely extensible nonlinear elastic (FENE), can be safely increased to at least 0.005τ , and although for the model used in this work larger timesteps can be used, it would hardly reach 0.005τ safely, therefore the difference in efficiency would be greater. The second comparison in Table 2 basically shows how much computational efficiency is lost by using the orientational potential to implement syndiotacticity as it is used in simulations of this work. The result shows only a $\sim 1.4\%$ difference when compared with the same model but atactic, that is, the intramolecular interactions that set this are deactivated (see Subsec. for details on this intramolecular interaction). Therefore, including tacticity in the model does not incur in a considerable computational expense. The last comparison in Table 2 in terms of computational performance was made for a melt composed of linear chains [100:0:1.5] and a system of SCLCPs [100:6:1.5] both with the same number of molecules, however, in the latter, there are more particles (112 cores in parallel are employed for this comparison). The linear polymeric chains of both systems are modeled with the same worm-like chain model, but the SCLCP system includes the syndiotactically attached spacers and the mesogenic units. Here, the difference in computational efficiency is about a $\sim 915\%$. This huge difference is due to the inclusion of mesogenic units modeled as uniaxial ellipsoids through the Gay-Berne potential, which is a very expensive potential and responsible for the decrease in computational performance, although one of the best options available to model anisotropic interactions. Finally, we have explored the computational scalability, performing simulations of SCLCP systems (for EOSC and SOSC configurations) with different numbers of cores, which is close to ideal.

Table 2: Comparison of the computational performance of different features of the SCLCP model. All the measurements are performed at $T = 8.0 \epsilon/k_B$, $P = 1.0 \epsilon/\sigma^3$, and a timestep of 0.002τ . The percentage difference is defined as how much efficient is the first system listed in comparison with the second system listed for each set of different comparisons.

| | | Computational performance |
|-----------------------------|-----------------------------------|---------------------------|
| System | linear (Kremer–Grest) [100:0:1.5] | 262135 τ /day |
| | linear [100:0:1.5] | 211329 τ /day |
| Percentage difference: 24% | | Number of cores: 56 |
| | | Computational performance |
| System | end-on [100:6:1.5] (atactic) | 15599 τ /day |
| | end-on [100:6:1.5] (syndiotactic) | 15380 τ /day |
| Percentage difference: 1.4% | | Number of cores: 56 |
| | | Computational performance |
| System | linear [100:0:1.5] | 328362 τ /day |
| | end-on [100:6:1.5] | 32356 τ /day |
| Percentage difference: 915% | | Number of cores: 112 |

CONCLUSION

In this work, we have developed a coarse-grained model for side-chain liquid crystal polymers. The model is well-defined in orientational terms, which allows constraints to be set to avoid unphysical rotation behavior of the mesogenic groups attached to the spacer chains, reproduce specific tacticity, and make the model responsive to external stimuli, such as external alignment fields. The model can be easily modified to implement different types of liquid crystalline sequences and compositions. The architectural flexibility of the model arises as a consequence of the increased degrees of freedom of its constituents, however, it is still computationally efficient enough to simulate large size and long time scales and, in particular, to study different LC mesophases. The model was tested with extensive simulations using standard parameters for nonbonded interactions and potentials in dimensionless units, and also standard parametrizations for ellipsoidal particles that reproduce the anisotropic behavior of mesogens. Although, the model has

the potential to map a specific chemistry. This is especially important since, as we are aware, this is the first coarse-grained model that can qualitatively reproduce the transition temperature difference between purely side-on and purely end-on configurations; by mapping to specific chemistry, we can move towards quantitative predictions of this transition. Finally, we can anticipate that the model will be useful to study a series of sequences and compositions of LC groups along the chain that can allow for a material with multiple types of deformations as a function of temperature. Different architectures, such as cross-linked bottlebrushes configurations will be explored in future work. These outcomes could serve as inspiration for applications with soft responsive materials.

Acknowledgement

Acknowledgment is made to the Donors of the American Chemical Society Petroleum Research Fund for support of this research. We also thank the Ohio Supercomputer Center for high-performance computing resources. (<http://osc.edu/ark:/19495/f5s1ph73>).⁸¹

Supporting Information Available

The data that support the findings of this study are available within the article and its supplementary material.

The external alignment field implemented as a fix⁶² for the LAMMPS package and its documentation https://dbecerra-dev.github.io/fix-ext_alignment are publicly available.

References

- (1) Allen, M. P.; Wilson, M. R. Computer simulation of liquid crystals. *Journal of Computer-Aided Molecular Design* **1989**, *3*, 335–353.

- (2) Lu, X.; Guo, S.; Tong, X.; Xia, H.; Zhao, Y. Tunable photocontrolled motions using stored strain energy in malleable azobenzene liquid crystalline polymer actuators. *Advanced Materials* **2017**, 29, 1606467.
- (3) Yang, R.; Zhao, Y. Multitemperature memory actuation of a liquid crystal polymer network over a broad nematic–isotropic phase transition induced by large Strain. *ACS Macro Letters* **2018**, 7, 353–357.
- (4) Bellin, I.; Kelch, S.; Langer, R.; Lendlein, A. Polymeric triple-shape materials. *Proceedings of the National Academy of Sciences* **2006**, 103, 18043–18047.
- (5) Ahir, S. V.; Tajbakhsh, A. R.; Terentjev, E. M. Self-assembled shape-memory fibers of triblock liquid-crystal polymers. *Advanced Functional Materials* **2006**, 16, 556–560.
- (6) Qin, H.; Mather, P. T. Combined one-way and two-way shape memory in a glass-forming nematic network. *Macromolecules* **2009**, 42, 273–280.
- (7) Ware, T. H.; Biggins, J. S.; Shick, A. F.; Warner, M.; White, T. J. Localized soft elasticity in liquid crystal elastomers. *Nature communications* **2016**, 7, 1–7.
- (8) Xu, Y.; Dupont, R. L.; Yao, Y.; Zhang, M.; Fang, J.-C.; Wang, X. Random Liquid Crystalline Copolymers Consisting of Prolate and Oblate Liquid Crystal Monomers. *Macromolecules* **2021**, 54, 5376–5387.
- (9) De Gennes, P. Possibilites offertes par la reticulation de polymeres en presence d'un cristal liquide. *Physics Letters A* **1969**, 28, 725–726.
- (10) Warner, M.; Terentjev, E. M. *Liquid crystal elastomers*; Oxford university press, 2007; Vol. 120.
- (11) Behl, M.; Lendlein, A. Shape-memory polymers. *Materials Today* **2007**, 10, 20–28.

- (12) Ahn, S.; Deshmukh, P.; Gopinadhan, M.; Osuji, C. O.; Kasi, R. M. Side-chain liquid crystalline polymer networks: exploiting nanoscale smectic polymorphism to design shape-memory polymers. *ACS Nano* **2011**, *5*, 3085–3095.
- (13) Shenoy, D. K.; Thomsen III, D. L.; Srinivasan, A.; Keller, P.; Ratna, B. R. Carbon coated liquid crystal elastomer film for artificial muscle applications. *Sensors and Actuators A: Physical* **2002**, *96*, 184–188.
- (14) Spillmann, C. M.; Naciri, J.; Martin, B. D.; Farahat, W.; Herr, H.; Ratna, B. R. Stacking nematic elastomers for artificial muscle applications. *Sensors and Actuators A: Physical* **2007**, *133*, 500–505.
- (15) Li, M. H.; Keller, P. Artificial muscles based on liquid crystal elastomers. *Philosophical Transactions of the Royal Society A: Mathematical, Physical and Engineering Sciences* **2006**, *364*, 2763–2777.
- (16) Kim, J. G.; Park, J. E.; Won, S.; Jeon, J.; Wie, J. J. Contactless manipulation of soft robots. *Materials* **2019**, *12*, 3065.
- (17) Wang, Y.; Liu, J.; Yang, S. Multi-functional liquid crystal elastomer composites. *Applied Physics Reviews* **2022**, *9*, 011301.
- (18) Kempe, M. D.; Scruggs, N. R.; Verduzco, R.; Lal, J.; Kornfield, J. A. Self-assembled liquid-crystalline gels designed from the bottom up. *Nature Materials* **2004**, *3*, 177–182.
- (19) Kempe, M. D.; Verduzco, R.; Scruggs, N. R.; Kornfield, J. A. Rheological study of structural transitions in triblock copolymers in a liquid crystal solvent. *Soft Matter* **2006**, *2*, 422–431.
- (20) Thakur, V. K.; Kessler, M. R., et al. *Liquid crystalline polymers*; Springer, 2016.

- (21) Moore, J.; Stupp, S. Orientation dynamics of main-chain liquid crystal polymers. 2. Structure and kinetics in a magnetic field. *Macromolecules* **1987**, *20*, 282–293.
- (22) Affouard, F.; Kröger, M.; Hess, S. Molecular dynamics of model liquid crystals composed of semiflexible molecules. *Physical Review E* **1996**, *54*, 5178.
- (23) Lyulin, A. V.; Al-Barwani, M. S.; Allen, M. P.; Wilson, M. R.; Neelov, I.; Allsopp, N. K. Molecular dynamics simulation of main chain liquid crystalline polymers. *Macromolecules* **1998**, *31*, 4626–4634.
- (24) Chen, W.; Zhu, Y.; Cui, F.; Liu, L.; Sun, Z.; Chen, J.; Li, Y. GPU-accelerated molecular dynamics simulation to study liquid crystal phase transition using coarse-grained gay-berne anisotropic potential. *PLOS One* **2016**, *11*, e0151704.
- (25) Cuierrier, E.; Ebrahimi, S.; Couture, O.; Soldera, A. Simulation of main chain liquid crystalline polymers using a Gay-Berne/Lennard-Jones hybrid model. *Computational Materials Science* **2021**, *186*, 110041.
- (26) Berardi, R.; Micheletti, D.; Muccioli, L.; Ricci, M.; Zannoni, C. A computer simulation study of the influence of a liquid crystal medium on polymerization. *The Journal of Chemical Physics* **2004**, *121*, 9123–9130.
- (27) Stimson, L. M.; Wilson, M. R. Molecular dynamics simulations of side chain liquid crystal polymer molecules in isotropic and liquid-crystalline melts. *The Journal of Chemical Physics* **2005**, *123*, 034908.
- (28) Collings, P. J.; Hird, M. *Introduction to liquid crystals chemistry and physics*; CRC Press, 2017.
- (29) Kannan, R. M.; Kornfield, J. A.; Schwenk, N.; Boeffel, C. Rheology of side-group liquid-crystalline polymers: effect of isotropic-nematic transition and evidence of flow alignment. *Macromolecules* **1993**, *26*, 2050–2056.

- (30) d'Allest, J.; Maissa, P.; Ten Bosch, A.; Sixou, P.; Blumstein, A.; Blumstein, R.; Teixeira, J.; Noirez, L. Experimental evidence of chain extension at the transition temperature of a nematic polymer. *Physical Review Letters* **1988**, *61*, 2562.
- (31) Wewerka, A.; Floudas, G.; Pakula, T.; Stelzer, F. Side-chain liquid-crystalline homopolymers and copolymers. Structure and rheology. *Macromolecules* **2001**, *34*, 8129–8137.
- (32) Wewerka, A.; Viertler, K.; Vlassopoulos, D.; Stelzer, F. Structure and rheology of model side-chain liquid crystalline polymers with varying mesogen length. *Rheologica Acta* **2001**, *40*, 416–425.
- (33) Rendon, S.; Burghardt, W. R.; Auad, M. L.; Kornfield, J. A. Shear-induced alignment of smectic side group liquid crystalline polymers. *Macromolecules* **2007**, *40*, 6624–6630.
- (34) Colby, R. H.; Gillmor, J.; Galli, G.; Laus, M.; Ober, C.; Hall, E. Linear viscoelasticity of side chain liquid crystal polymer. *Liquid Crystals* **1993**, *13*, 233–245.
- (35) Pleiner, H.; Brand, H. R. Local rotational degrees of freedom in nematic liquid-crystalline side-chain polymers. *Macromolecules* **1992**, *25*, 895–901.
- (36) Fourmaux-Demange, V.; Brûlet, A.; Cotton, J.; Hilliou, L.; Martinoty, P.; Keller, P.; Boué, F. Rheology of a comblike liquid crystalline polymer as a function of its molecular weight. *Macromolecules* **1998**, *31*, 7445–7452.
- (37) Long, D.; Morse, D. C. A Rouse-like model of liquid crystalline polymer melts: Director dynamics and linear viscoelasticity. *Journal of Rheology* **2002**, *46*, 49–92.
- (38) Wang, X.; Warner, M. Theory of nematic comb-like polymers. *Journal of Physics A: Mathematical and General* **1987**, *20*, 713.

- (39) Renz, W.; Warner, M. The theory of competing nematic phases of comb polymers. *Proceedings of the Royal Society of London. A. Mathematical and Physical Sciences* **1988**, *417*, 213–233.
- (40) Brochard, F.; Jouffroy, J.; Levinson, P. Phase diagrams of mesomorphic mixtures. *Journal de Physique* **1984**, *45*, 1125–1136.
- (41) Chiu, H.-W.; Kyu, T. Equilibrium phase behavior of nematic mixtures. *The Journal of Chemical Physics* **1995**, *103*, 7471–7481.
- (42) Kim, N.; Choi, J.; Chien, L.-C.; Kyu, T. Phase equilibria of a mixture of side-chain liquid crystalline polymer and low molecular mass liquid crystal. *Macromolecules* **2007**, *40*, 9582–9589.
- (43) Carri, G. A.; Muthukumar, M. Configurations of liquid crystalline polymers in nematic solvents. *The Journal of Chemical Physics* **1998**, *109*, 11117–11128.
- (44) Wang, R.; Wang, Z.-G. Theory of side-chain liquid crystal polymers: Bulk behavior and chain conformation. *Macromolecules* **2010**, *43*, 10096–10106.
- (45) Pasini, P.; Chiccoli, C.; Zannoni, C. *Advances in the Computer Simulations of Liquid Crystals*; Springer, 2000; pp 121–138.
- (46) Wilson, M. R.; Yu, G.; Potter, T. D.; Walker, M.; Gray, S. J.; Li, J.; Boyd, N. J. Molecular simulation approaches to the study of thermotropic and lyotropic liquid crystals. *Crystals* **2022**, *12*, 685.
- (47) Wilson, M. R. Molecular dynamics simulations of flexible liquid crystal molecules using a Gay-Berne/Lennard-Jones model. *The Journal of Chemical Physics* **1997**, *107*, 8654–8663.
- (48) McBride, C.; Wilson, M. R. Molecular dynamics simulations of a flexible liquid crystal. *Molecular Physics* **1999**, *97*, 511–522.

- (49) Wilson, M. R.; Ilnytskyi, J. M.; Stimson, L. M. Computer simulations of a liquid crystalline dendrimer in liquid crystalline solvents. *The Journal of Chemical Physics* **2003**, *119*, 3509–3515.
- (50) Ilnytskyi, J. M.; Neher, D. Structure and internal dynamics of a side chain liquid crystalline polymer in various phases by molecular dynamics simulations: A step towards coarse graining. *The Journal of Chemical Physics* **2007**, *126*, 174905.
- (51) Ilnytskyi, J. M.; Saphiannikova, M.; Neher, D.; Allen, M. P. Modelling elasticity and memory effects in liquid crystalline elastomers by molecular dynamics simulations. *Soft Matter* **2012**, *8*, 11123–11134.
- (52) Gay, J.; Berne, B. Modification of the overlap potential to mimic a linear site–site potential. *The Journal of Chemical Physics* **1981**, *74*, 3316–3319.
- (53) Cleaver, D. J.; Care, C. M.; Allen, M. P.; Neal, M. P. Extension and generalization of the Gay-Berne potential. *Physical Review E* **1996**, *54*, 559.
- (54) Allen, M. P.; Warren, M. A.; Wilson, M. R.; Sauron, A.; Smith, W. Molecular dynamics calculation of elastic constants in Gay–Berne nematic liquid crystals. *The Journal of Chemical Physics* **1996**, *105*, 2850–2858.
- (55) Ilnytskyi, J. M.; Neher, D.; Saphiannikova, M. Opposite photo-induced deformations in azobenzene-containing polymers with different molecular architecture: Molecular dynamics study. *The Journal of Chemical Physics* **2011**, *135*, 044901.
- (56) Ilnytskyi, J.; Wilson, M. R. A domain decomposition molecular dynamics program for the simulation of flexible molecules with an arbitrary topology of Lennard–Jones and/or Gay–Berne sites. *Computer Physics Communications* **2001**, *134*, 23–32.
- (57) Ilnytskyi, J. M.; Wilson, M. R. A domain decomposition molecular dynamics program for the simulation of flexible molecules of spherically-symmetrical and non-

- spherical sites. II. Extension to NVT and NPT ensembles. *Computer Physics Communications* **2002**, *148*, 43–58.
- (58) Chirico, G.; Langowski, J. Kinetics of DNA supercoiling studied by Brownian dynamics simulation. *Biopolymers: Original Research on Biomolecules* **1994**, *34*, 415–433.
- (59) Brackley, C. A.; Morozov, A. N.; Marenduzzo, D. Models for twistable elastic polymers in Brownian dynamics, and their implementation for LAMMPS. *The Journal of Chemical Physics* **2014**, *140*, 04B603_1.
- (60) Lequeieu, J.; Córdoba, A.; Moller, J.; De Pablo, J. J. 1CPN: A coarse-grained multi-scale model of chromatin. *The Journal of Chemical Physics* **2019**, *150*, 215102.
- (61) Thompson, A. P.; Aktulga, H. M.; Berger, R.; Bolintineanu, D. S.; Brown, W. M.; Crozier, P. S.; in 't Veld, P. J.; Kohlmeyer, A.; Moore, S. G.; Nguyen, T. D.; Shan, R.; Stevens, M. J.; Tranchida, J.; Trott, C.; Plimpton, S. J. LAMMPS - a flexible simulation tool for particle-based materials modeling at the atomic, meso, and continuum scales. *Computer Physics Communications* **2022**, *271*, 108171.
- (62) Becerra, D.; Hall, L. M. <https://github.com/hall-polymers/SCLCP>, 2022.
- (63) Community, B. O. Blender - a 3D modelling and rendering package. Blender Foundation: Stichting Blender Foundation, Amsterdam, 2018.
- (64) Berardi, R.; Fava, C.; Zannoni, C. A Gay–Berne potential for dissimilar biaxial particles. *Chemical Physics Letters* **1998**, *297*, 8–14.
- (65) Everaers, R.; Ejtehadi, M. Interaction potentials for soft and hard ellipsoids. *Physical Review E* **2003**, *67*, 041710.
- (66) Bates, M.; Luckhurst, G. Computer simulation studies of anisotropic systems. XXX. The phase behavior and structure of a Gay–Berne mesogen. *The Journal of Chemical Physics* **1999**, *110*, 7087–7108.

- (67) Adams, D.; Luckhurst, G.; Phippen, R. Computer simulation studies of anisotropic systems: XVII. The Gay-Berne model nematogen. *Molecular Physics* **1987**, *61*, 1575–1580.
- (68) Emsley, J.; Luckhurst, G.; Palke, W.; Tildesley, D. Computer simulation studies of the dependence on density of the orientational order in nematic liquid crystals. *Liquid Crystals* **1992**, *11*, 519–530.
- (69) de Miguel, E.; Rull, L. F.; Gubbins, K. E. Dynamics of the Gay-Berne fluid. *Physical Review A* **1992**, *45*, 3813.
- (70) Moreno-Razo, J. A.; Sambriski, E.; Koenig, G. M.; Díaz-Herrera, E.; Abbott, N. L.; De Pablo, J. Effects of anchoring strength on the diffusivity of nanoparticles in model liquid-crystalline fluids. *Soft Matter* **2011**, *7*, 6828–6835.
- (71) Luckhurst, G.; Stephens, R.; Phippen, R. Computer simulation studies of anisotropic systems. XIX. Mesophases formed by the Gay-Berne model mesogen. *Liquid Crystals* **1990**, *8*, 451–464.
- (72) Berardi, R.; Emersont, A. P.; Zannoni, C. Monte Carlo Investigations of a Gay-Berne Liquid Crystal. *Journal of the Chemical Society, Faraday Transactions* **1993**, *89*, 4069–4078.
- (73) Brown, W. M.; Petersen, M. K.; Plimpton, S. J.; Grest, G. S. Liquid crystal nanodroplets in solution. *The Journal of Chemical Physics* **2009**, *130*, 044901.
- (74) Margola, T.; Satoh, K.; Saielli, G. Comparison of the mesomorphic behaviour of 1: 1 and 1: 2 mixtures of charged Gay-Berne GB (4.4, 20.0, 1, 1) and Lennard-Jones particles. *Crystals* **2018**, *8*, 371.
- (75) Bobbili, S. V.; Milner, S. T. Simulation study of entanglement in semiflexible polymer melts and solutions. *Macromolecules* **2020**, *53*, 3861–3872.

- (76) Stukowski, A. Visualization and analysis of atomistic simulation data with OVITO—the Open Visualization Tool. *Modelling and Simulation in Materials Science and Engineering* **2009**, *18*, 015012.
- (77) Klüppel, M. Characterization of nonideal networks by stress-strain measurements at large extensions. *Journal of Applied Polymer Science* **1993**, *48*, 1137–1150.
- (78) Ren, W.; McMullan, P. J.; Griffin, A. C. Poisson’s ratio of monodomain liquid crystalline elastomers. *Macromolecular Chemistry and Physics* **2008**, *209*, 1896–1899.
- (79) Mottram, N. J.; Newton, C. J. Introduction to Q-tensor theory. *arXiv preprint arXiv:1409.3542* **2014**,
- (80) Kremer, K.; Grest, G. S. Dynamics of entangled linear polymer melts: A molecular-dynamics simulation. *The Journal of Chemical Physics* **1990**, *92*, 5057–5086.
- (81) Center, O. S. Ohio Supercomputer Center. 1987;
<http://osc.edu/ark:/19495/f5s1ph73>.